International Astronautical Congress, Dubai, United Arab Emirates, 25-29 October 2021.


IAC-21-A3-2B-3-x63042

# Control System Design for the ALINA Lunar Lander

**Jose Luis Redondo Gutierrez**[a]*, **Stefano Farì**[a], **Matthias Winter**[a]

[a] *German Aerospace Center (DLR), Institute of Space Systems, Department of Navigation and Control Systems, Robert-Hooke-Str. 7, 28359, Bremen, Germany.* E-mail: Jose.RedondoGutierrez@dlr.de, Stefano.Fari@dlr.de, Matthias.Winter@dlr.de

* Corresponding author

**Abstract**

This paper presents the control system developed by the German Aerospace Center (DLR) for the ALINA lunar lander. The control system is part of the overall Guidance, Navigation and Control (GNC) subsystem. ALINA, developed by Planetary Transportation Systems GmbH (PTS), is a spacecraft able to semi-autonomously perform a complete Earth to lunar surface mission and to deliver up to 200 kg of payload. The control system has successfully passed the project's Preliminary Design Review (PDR). The vehicle, the mission phases and objectives as well as the control requirements are introduced, and the adopted control solutions presented. Of major importance is the spacecraft's propulsion configuration: it comprises a cluster of throttlable and non-throttlable main engines, as well as attitude control thrusters, fed by several propellant tanks. Therefore, specific challenges arise, such as control allocation and propellant sloshing. The synthesis of the controllers employs optimal control techniques to design the control laws for the different GNC tasks, including detumbling, single-axis pointing, three-axis pointing, maneuver execution, and powered descent, Hazard Detection and Avoidance (HDA) and landing. Attention has been given to the translational and rotational dynamics couplings, as the individual engines do not provide thrust vector control capabilities. The control allocation problem is tackled by minimizing a cost function that takes into account the desired forces and torques, as well as the fuel consumption; the online solution is found by transcribing the problem into a linear programming form and solving it using the SIMPLEX method. Propellant sloshing can disturb thrust vector pointing and can potentially generate critical deviations from the nominal trajectory and instabilities, particularly, as initially more than 70 % of the spacecraft mass consists of fuel. Therefore, the plant model includes a representation of propellant sloshing dynamics using mechanical analogies. This has been achieved using the multi-physics object-oriented modeling language Modelica, better suited for large multibody representations; the resulting implementation is consequently embedded within a high-fidelity simulation framework. For the verification process, the control system has been included in the latter. Representative Monte-Carlo campaigns were conducted, with a dedicated focus on the powered descent, HDA and landing. The analysis of the control performance throughout each mission phase shows a good overall performance, well complying with all applicable requirements.

## Nomenclature

In this paper, the mathematical typesetting adopts the following notation: (i) scalars with non-bold, italic, small letter characters; (ii) vectors with bold, non-italic, small letter characters; (iii) matrices with bold, non-italic, capital letter characters; (iv) ${}^{\mathtt{C}}_{\mathtt{A},\mathtt{B}}\mathbf{r}_{\mathrm{id}_i}$ expresses a vector referenced to frame A, with respect to frame B, projected in frame C, 'id' is a descriptive identifier and '$i$' is an index (e.g. the index of a thruster).

## 1. Introduction

With the Commercial Lunar Payload Services (CLPS) Program by NASA, China's on-going Chang'e Program, the ESA decision to start the robotic exploration of the lunar surface and several other lunar programs by state and private actors, the development of efficient and reliable means to precisely land payloads on the lunar surface has become a major topic. Also in the scope of manned programs like the US-led Artemis Program, autonomous deliv-

ery of large amounts of payload is needed to support the establishment of temporary or permanent lunar bases.

This paper presents the design of the control system for the ALINA spacecraft. ALINA is the combined transfer stage and Moon lander under development by the NewSpace company PTS [1, 2] and has a payload capacity of 200 kg, a dry mass of 1150 kg and a wet mass of just over 4 t. Originating from the Google Lunar X Prize, from which the project received a total of $750,000 of prize money, PTS plans to perform the first European landing on the Moon in the early 2020s to conduct science experiments (e.g. in-situ resource utilization) and technology demonstrations as well as to deliver commercial payloads. Since ALINA is not meant to be used for a one-off mission but for a series of lunar missions, the design is kept generic to allow for different payloads and landing sites. The control system is part of the overall AOCS/GNC system developed by DLR and PTS [3].

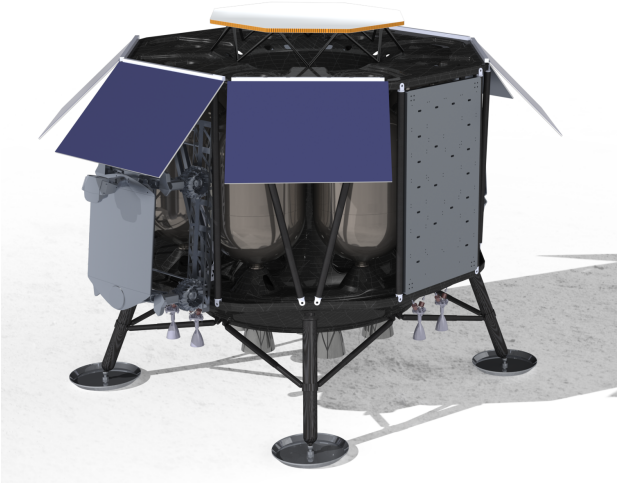

Fig. 1: Rendering of ALINA (courtesy PTS GmbH)

The control system described in this paper contains the control function and the actuator management. First, the overall mission (section 2) and the GNC system (section 3 and 4) are introduced. This is followed by a more detailed description of the propulsion system and the potential effects of propellant sloshing in section 5. After those initial sections, the focus is put on the design of the control function, explaining in detail the controllers developed for each phase of the mission (section 6). Section 7 explains how the control allocation problem is solved, transforming the commanded forces and torques into commands to the actuators. The simulation environment used to study the performance of the different controllers is then briefly explained (section 8). Finally, some simulation results are shown to provide an overview about the behavior of the system (section 9).

## 2. Mission

The Cruise & Orbital Phase (COP) starts at launcher separation. A phasing orbit strategy with several apogee raising maneuvers is used to bring ALINA from a highly-elliptical orbit with an apogee altitude of about 80 000 km to the lunar altitude of 405 000 km. After the final apogee raising maneuver – the Trans-Lunar Injection (TLI) –, the Lunar Transfer Orbit (LTO) is entered. After the Lunar Orbit Injection (LOI), ALINA gets captured by Moon gravity into a highly-elliptical lunar orbit with a periselene of 6500 km. A series of circularization maneuvers are used to bring ALINA into a 100 km retrograde parking orbit. Here, orbital payloads are operated. As start of the landing operations, the Descent Orbit Injection (DOI) is performed to move ALINA into the 100 km x 15 km Descent Orbit (DO). Several revolutions are performed in this orbit for sensor and navigation filter checkouts (in particular of Crater Navigation (CNav)). Approximately one Earth-day after local sunrise at the landing site, the Powered Descent, HDA & Landing (PDHL) will be initiated near the periselene.

The landing site for the first mission is at E 30.61436°, N 20.1960°, located at a distance of about 4.5 km west of the Apollo 17 landing site. Due to Mission and GNC constraints, the landing is planned for shortly after 6.81 h Local True Solar Time (LTST). Figure 2 shows the landing ellipse of 500 m by 750 m. The red dashed line shows the incoming trajectory of ALINA (103° orbital inclination) and the gray dashed line shows the direction towards the Apollo 17 site. [3]

## 3. Driving GNC Requirements

Driving requirements for the overall GNC system are the need for complete autonomy during the landing phase and delta-v maneuvers, the required absolute landing accuracy of 500 m (along-track) by 750 m (cross-track) and the touch down conditions (i.e. horizontal speed $< 2$ m/s, vertical speed $< 4$ m/s, yaw/pitch angle $< 10°$). Moreover, the nature of a

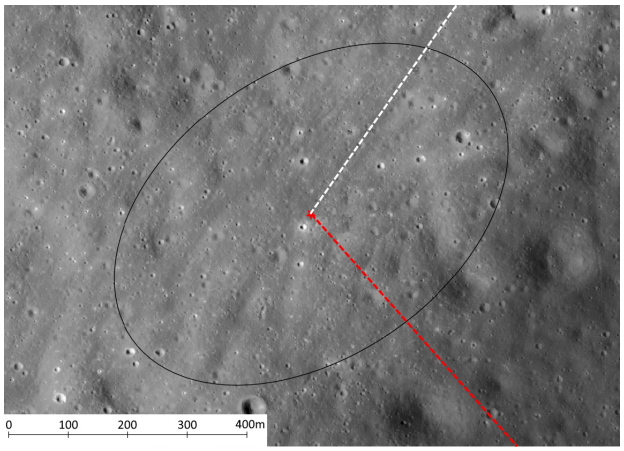


Fig. 2: Orthomosaic map of the landing site for the first mission (courtesy PTS GmbH)

| AOCS Mode | Objectives |
|---|---|
| Detumbling Mode (DTM) | Reduce angular rates to required target conditions |
| Acquisition and Safe Mode (ASM) | Acquire and keep safe attitude |
| Three-Axis Mode (TAM) | Point spacecraft to defined attitude in inertial or orbital frame |
| Maneuver Execution Mode (MEM) | Realise delta-v maneuvers |
| Transfer Mode (TFM) | Slow rotation around roll axis for thermal reasons |
| Powered Descent Mode (PDM) | Follow descent trajectory and execute HDA, final approach and landing |

Table 1: AOCS Modes

non-abortable landing maneuver sets strong demands on the robustness and fault-tolerance of hardware and software, especially as safe mode occurrences or reboots of the main computer are not an option during this critical phase. Finally, as the mission baseline requires extensive delta-v, about 70 % of ALINA's initial mass is propellant. This means that the mass, inertia and center of mass of the spacecraft are strongly changing over the mission duration and that sloshing effects need to be considered in the design. [3]

## 4. GNC Architecture

The Attitude and Orbital Control System (AOCS) modes and their respective objectives are presented in Table 1.

The overall GNC architecture and the interfaces of the control system are shown in Figure 3 (for attitude control) and Figure 4 (for PDHL).

For pure attitude control, the control function receives the current attitude and angular rate targets from the guidance algorithms and the current attitude and angular rate estimates from the navigation filter. The control function outputs the demanded control torques to the actuator management function, which then outputs the actuator commands to the attitude control thrusters. The Mission Vehicle Management (MVM) includes the mode logic and selects the appropriate controller and actuator management functions.

For the PDHL, the controller receives the current position, velocity, attitude and angular rate targets as well as feedforward accelerations (translational and angular) from the guidance algorithms. The control function outputs the demanded torques and forces to the actuator management function, which then outputs the actuator commands to the main engines and attitude control thrusters.

A more detailed description of the overall GNC architecture, a design overview for all major algorithmic areas and system-level test results are presented in a dedicated paper [3].

## 5. Vehicle

ALINA is a combined transfer stage and Moon lander [1, 2] and has a payload capacity of 200 kg, a dry mass of 1150 kg and a wet mass just over 4 t.

### *5.1 Propulsion system*

The attitude control thrusters are the sole actuators for attitude control while no delta-v maneuvers are executed. During delta-v maneuvers, including the powered descent and landing, they are also used as supporting attitude actuators. There are a total of eight 10 N thrusters, two pairs under the baseplate and two pairs on top of the lander (see Figure 5). They allow pure-torque generation (i.e. realization of torques without resulting force).

The main engine assembly is used during delta-v maneuvers and Powered Descent, HDA & Landing (PDHL). It consists of seven non-pulsable 420 N and eight pulsable 245 N engines, all aligned along the $-\mathbf{x}_B$-axis (roll) of the spacecraft (see Fig 5). The

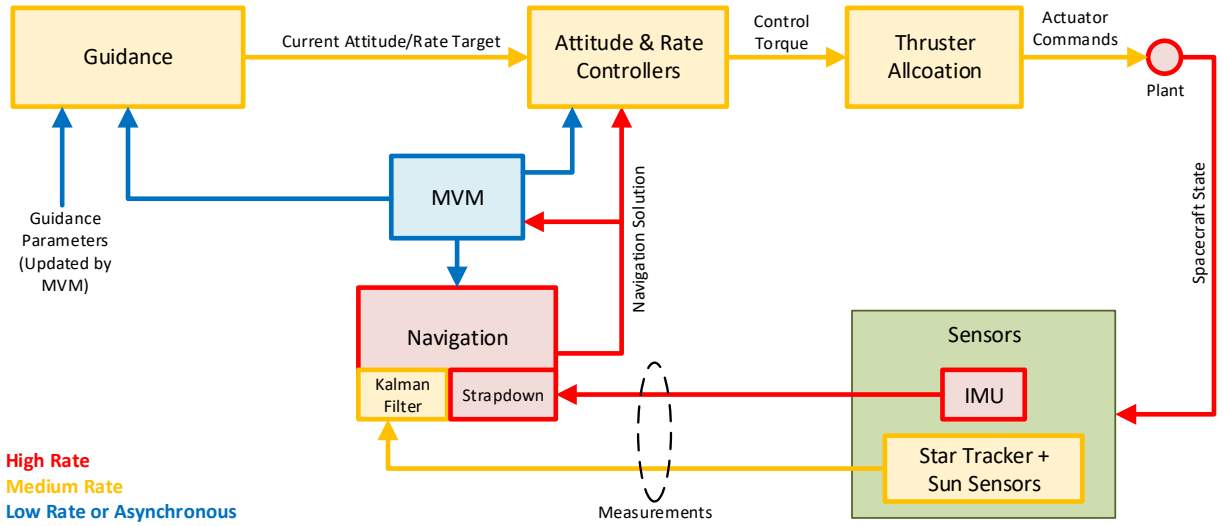


Fig. 3: 3-DoF Attitude Control Loop for Cruise & Orbital Phase (COP)

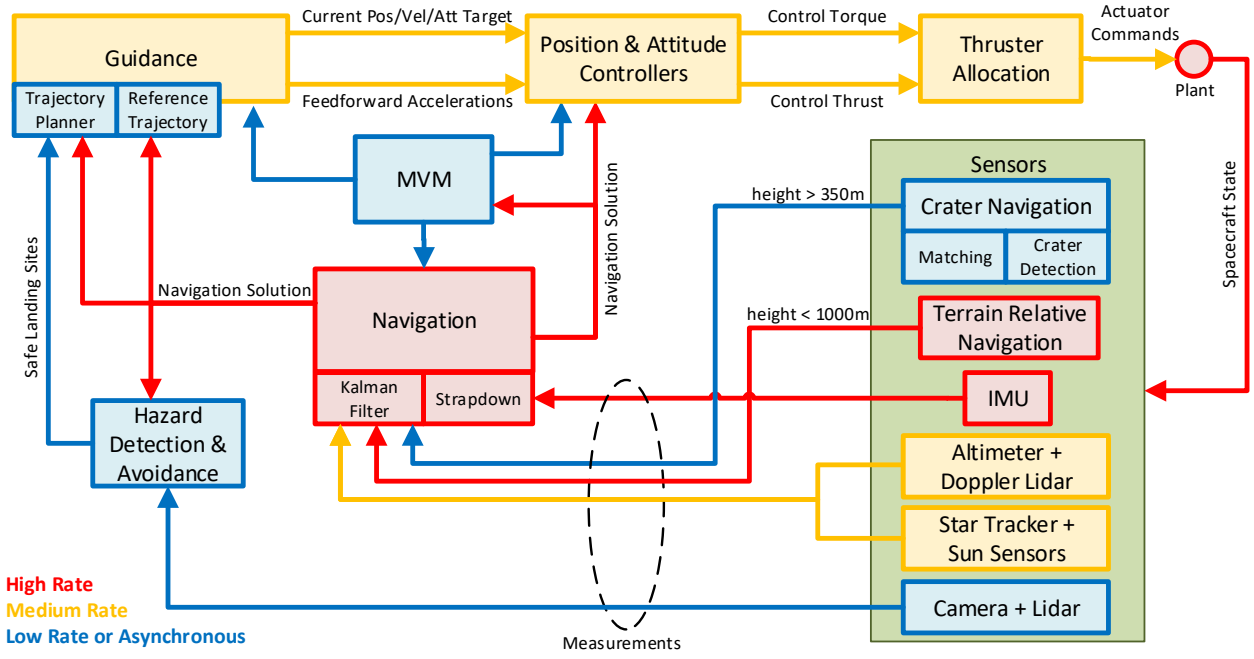


Fig. 4: 6-DoF Position/Attitude Control Loop for Descent, HDA and Landing Phase (PDHL)

maximum total thrust accumulates to 4900 N. The decision to use two different types of main engines is based on the consideration that non-pulsable engines can generally deliver higher specific impulse but that during the powered descent, pulsable engines are needed as well to control the thrust magnitude and to compensate the large disturbance torques along the pitch and yaw axes, which are induced by the main engines and the offset between center of mass and center of thrust. The alternative approach of sizing the

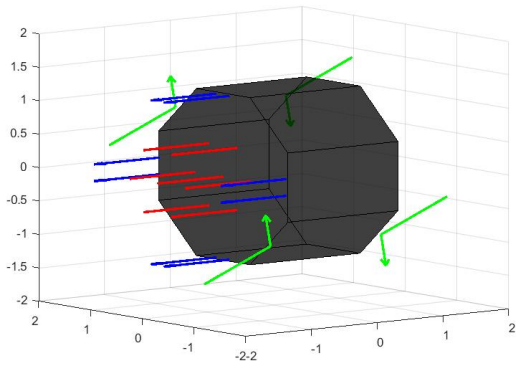

Fig. 5: Propulsion system. Attitude thrusters (green), non-pulsable main engines (red), pulsable main engines (blue)

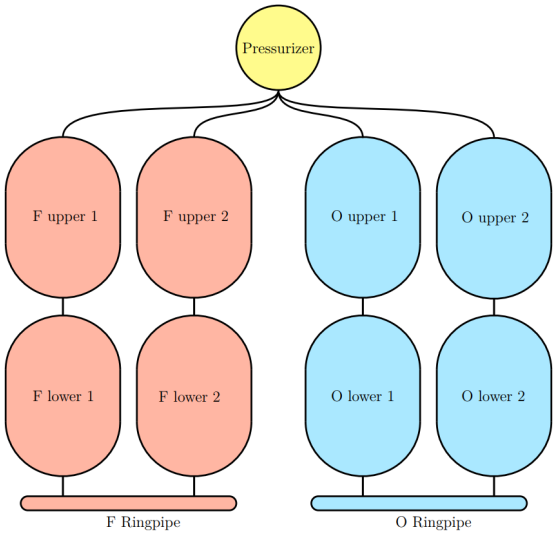


Fig. 6: ALINA tank system schematic (simplified)

attitude control thrusters such that they can compensate these disturbances torques, would require much stronger attitude control thrusters, of which some would need to be accommodated on top of the spacecraft. Moreover, fuel consumption would increase, as a much larger part of the thrust would not be utilized for the planned delta-v generation. To minimize disturbance torque generation, the non-pulsable engines are located as an inner ring plus a central engine under the baseplate of the spacecraft. To maximize the control torque capabilities, the pulsed 245 N engines are situated on the outside of the baseplate. The approach of using a small cluster of medium-sized engines was chosen to eliminate the use of larger, throttleable and gimballed engines. This simplifies the spacecraft design and cost and allows for greater redundancy.

As the total required delta-v for the mission is quite large, ALINA will carry about 2850 kg of propellant. The propellants employed for the engine combustion are Mixed Oxides of Nitrogen (MON) as oxidizer and Monomethylhydrazine (MMH) as fuel, stored in eight tanks. The same tank model is used for oxidizer and fuel to save development costs and to create a balanced dry vehicle structure. The oxidizer to fuel mass ratio of the ALINA spacecraft is chosen such that the total oxidizer volume equals the total fuel volume.

The tanks are connected in the way illustrated in Figure 6. There are two distribution rings, which deliver the propellant to the main engines. The overall system is pressurized with Helium, stored in a spherical tank placed on the vehicle's roll axis ($\mathbf{x}_B$). The details of the tanks are provided in Table 2.

In the simulation environment, the dynamic state of each tank is obtained by means of a suitable model, which accounts for this specific tank configuration. These states include: remaining mass, tank center of mass, estimated liquid moment of inertia, and filling height. This aspect is covered in a dedicated publication in more detail [4], along with the control logic employed to avoid fuel imbalances.

### *5.2 Propellant sloshing dynamics*

The spacecraft mass is composed of more than 70 % of liquid; this implies that the vehicle will experience disturbances generated by the internal propellant sloshing dynamics during and after every accelerating maneuver. Sloshing dynamics, if not appropriately addressed, may drastically increase the trajectory tracking error [5]. Therefore, the control algorithms need to be validated within an appropriate simulation frameworks able to capture sloshing effect on the spacecraft dynamics. Equivalent mechanical models can approximate sloshing under specific assumptions, allowing the derivation of the vehicle's equations of motion [6–8]. However, while suitable for analysis and control synthesis purposes, this approach presents several limitations for implementation as a simulation model. This limitations are particularly relevant for vehicle configurations with several tanks like ALINA, and cases for which several

| Tank nr. | Fluid type | Tank shape | Sloshing modes | Capacity | Notes |
|---|---|---|---|---|---|
| 1-4 | MON | Cyl. with half spherical domes | 3 | >450kg | - |
| 5-8 | MMH | Cyl. with half spherical domes | 3 | >280kg | - |
| 9 | He | Spherical | 0 | <20kg | Pressurizer |
| 10 | MON | Toroidal | 0 | <0.5kg | Distribution ring |
| 11 | MMH | Toroidal | 0 | <0.5kg | Distribution ring |

Table 2: ALINA tank system configuration

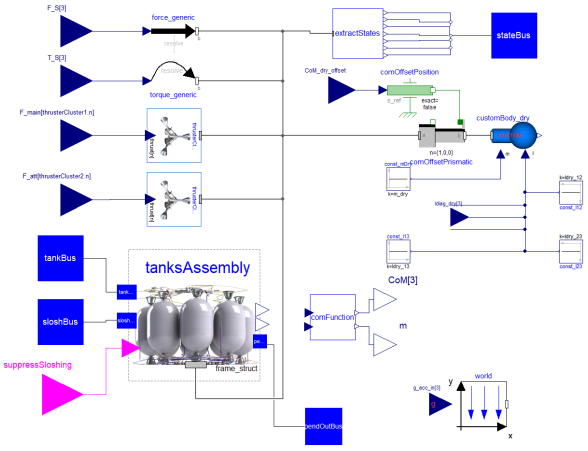


Fig. 7: VLVLib superclass for vehicle with sloshing dynamics simulation

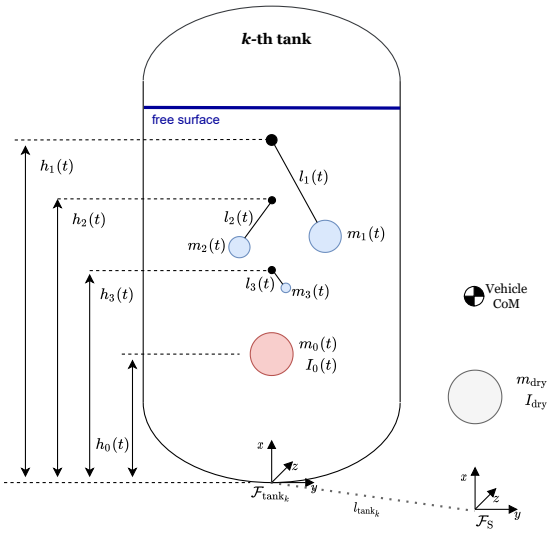


Fig. 8: Representation of the employed sloshing equivalent model

sloshing modes have to be considered. Here, a flexible framework is used to enable high-fidelity simulations of the sloshing phenomenon for the verification of the GNC algorithms. The multibody plant embedding slosh dynamics is modeled by means of DLR's Vertical Landing Vehicles Library (VLVLib), written using the object-oriented Modelica modeling language [9].

The development requirements for the model were:

1. The vehicle model shall address the sloshing phenomenon without altering the single tanks MCI (Mass, Center of Mass, Inertia) static properties (see Eqs. 1 and 2);
2. the model shall not make any planar motion assumption;
3. the fuel draining effect shall be considered, i.e. all modeled masses shall be time-varying;
4. the capability of including up to three sloshing modes per tank shall be given;

In Figure 7, the Modelica model superclass is shown. This compiled object is then embedded in the main simulation environment for GNC algorithm verification. The class instantiates the eight tank models which include the three pendula dynamics (one per sloshing mode) and three tank classes for which fuel sloshing is not activated (Table 2).

Figure 8 illustrates the tank model together with the main reference frames. The model distinguishes between the sloshing and the non-sloshing parts of the liquid: the liquid mass $m_{\text{liq}}$ is split between the single pendulum masses $m_i$, with $i \in [1,2,3]$ being the sloshing mode, and the mass $m_0$ representing the idle liquid. Furthermore, $h_0$ and $h_i$ are the non-sloshing body and the $i$-th pendulum hinge height with respect to the bottom of the tank; $m_i$ and $l_i$ are the mass and arm length of the $i$-th pendulum. Parameters $m_0$, $I_0$, $h_i$, $l_i$ and $m_i$ are provided with respect to discrete tank filling levels and have to be interpolated during the simulation. The frame $\mathscr{F}_{\text{S}}$ is a vehicle-structure-fixed frame conveniently chosen, whereas $\mathscr{F}_{\text{tank}_k}$ is a frame at the bottom point of the $k$-th tank, with $k = 1,2,...,K$. The whole liquid inertia in a tank $I_0$ is

considered and placed together with the non-sloshing mass $m_0$. The gray body in Figure 8 models the dry vehicle: the mass and moment of inertia have been labeled with $m_{\text{dry}}$ and $I_{\text{dry}}$. The depicted position of the overall vehicle's center of mass is influenced by the idle masses distribution, but also by each pendulum motion.

To ensure the model validity, the static properties of the liquid must be preserved at every time instant for every $k$-th tank. Hence,

$$m_0 + \sum_i m_i = m_{\text{liq}}, \tag{1}$$

$$m_0 h_0 + \sum_i m_i h_i = 0. \tag{2}$$

Despite Figure 8 planar depiction, each modeled pendulum is enabled to move in three dimensions.

Damping is included as well as function of the vehicle longitudinal acceleration and the damping coefficient. The latter is derived by the tank shape and liquid properties and is not further described here [10].

## 6. Control Design

The control system is meant to track the reference state defined by the guidance, by generating the necessary forces and torques signals to be realized by the actuators. The goal is to robustly track the reference with a determined accuracy, using the state estimation provided by the navigation filter.

Even though the specific requirements of the different AOCS modes require designing distinct controllers, there is a series of control strategies and tools that are recurrently used. The first step in the control design is to define the equations that represent the dynamics of the motion to be controlled. These are non-linear equations that depend on the state, the control input and the mass of the vehicle. In order to apply linear control synthesis techniques, this set of non-linear equations is linearized around a set of points ($i$), determined by the mass and the state:

$$\dot{\mathbf{x}} = F(\mathbf{x}, \mathbf{u}, m) \quad \rightarrow \quad \dot{\mathbf{x}}_i = \mathbf{A}_i(\mathbf{x} - \mathbf{x}_i) + \mathbf{B}_i \mathbf{u} \tag{3}$$

where $\mathbf{x}$ is the state vector, $\mathbf{u}$ the input vector, $\mathbf{A}$ the state matrix and $\mathbf{B}$ the input matrix. The resulting linear systems, defined by $\mathbf{A}_i$, $\mathbf{B}_i$ and $\mathbf{x}_i$, are linked to a particular state and mass of the vehicle, and therefore undergo considerable changes during the mission.

For each linear plant a feedback controller is obtained using Linear Quadratic Regulator (LQR) synthesis, determining the gain matrix $\mathbf{K}$ such that the cost function $J$ is minimized:

$$\mathbf{u} = -\mathbf{K}\Delta\mathbf{x} \tag{4}$$

$$J = \int_0^\infty (\Delta\mathbf{x}^T \mathbf{Q} \Delta\mathbf{x} + \mathbf{u}^T \mathbf{R}\, \mathbf{u} + 2\Delta\mathbf{x}^T \mathbf{N}\, \mathbf{u}) dt \tag{5}$$

where matrices $\mathbf{Q}$, $\mathbf{R}$ and $\mathbf{N}$ are defined for each controller, depending on the particular requirements.

The control gains are then interpolated from these sets of gains using the mass of the vehicle as the interpolating variable. All controllers include a deadband to avoid unnecessary thruster firings when the error signal is small. The rest of this section explains the controllers, which are shown in Table 3.

| AOCS Mode | Controller | DoF |
|---|---|---|
| DTM | angular rate | Rot. |
| ASM/TFM | single-axis | Rot. |
| TAM | three-axes | Rot. |
| MEM | delta-v | Rot. + Transl. |
| PDM | 6-DoF | Rot. + Transl. |

Table 3: Controller type for each AOCS mode.

### *6.1 Cruise and Orbital Phase*

The attitude dynamics model used to design the attitude controllers is

$${}^{\mathtt{B}}_{\mathtt{R}}\dot{\mathbf{q}} = \frac{1}{2}\,\Omega\, {}^{\mathtt{B}}_{\mathtt{R}}\mathbf{q} \tag{6}$$

$${}^{\mathtt{B}}_{\mathtt{B,R}}\dot{\boldsymbol{\omega}} = \mathbf{I}^{-1}({}^{\mathtt{B}}\boldsymbol{\tau} - {}^{\mathtt{B}}_{\mathtt{B,R}}\boldsymbol{\omega} \times \mathbf{I} \cdot {}^{\mathtt{B}}_{\mathtt{B,R}}\boldsymbol{\omega}) \tag{7}$$

where $\mathtt{R}$ is the current guidance reference frame (which can be an inertial or an orbital frame), $\mathtt{B}$ the body reference frame, ${}^{\mathtt{B}}_{\mathtt{B,R}}\boldsymbol{\omega}$ the angular rate of $\mathtt{B}$ with respect to $\mathtt{R}$ expressed in $\mathtt{B}$, $\Omega = [{}^{\mathtt{B}}_{\mathtt{B,R}}\boldsymbol{\omega}\otimes]$ the extended angular rate [11], ${}^{\mathtt{B}}_{\mathtt{R}}\mathbf{q}$ the quaternion describing the rotation from $\mathtt{R}$ to $\mathtt{B}$, ${}^{\mathtt{B}}\boldsymbol{\tau}$ the torque in $\mathtt{B}$, and $\mathbf{I}$ the inertia matrix. Below, frames are omitted in the control laws for conciseness; quantities are expressed always in $\mathtt{B}$ frame.

The DTM controller aims at detumbling the spacecraft after separation from the launcher, bringing the inertially-referenced ${}^{\mathtt{B}}_{\mathtt{B,R}}\boldsymbol{\omega}$ to zero. As this controller does not aim at controlling the attitude of the vehicle, only equation 7 is used for the LQR synthesis, leading to an expression for the demanded control torque as:

$$\boldsymbol{\tau}_{\text{dmd}} = -\mathbf{K}\,\boldsymbol{\omega} \tag{8}$$

Here, $\mathbf{K}$ is obtained considering a fully-fueled vehicle.

The single-axis controller used for ASM and TFM aims at reaching and maintaining a defined angle between a chosen axis of the spacecraft and a defined axis in the current guidance reference frame (e.g. inertial or orbital). Two applications are: 1) reaching a safe attitude with a sufficient amount of sun light captured by the solar arrays, while minimizing the spacecraft rotation about the spacecraft-sun axis, and 2) slowly rotating around the spacecraft roll-axis with a reference axis such that the different sides of ALINA receive equal amount of heat input from the Sun while avoiding start tracker blinding. The inputs to this controller are: 1) the estimated mass, used to interpolate the control gains, 2) the estimated angular rate and orientation of the vehicle axes, and 3) the commanded angular rate, pointing axis and the corresponding angle w.r.t. the pointing axis. The controller computes the principal rotation vector [11] that will bring ALINA to point in the demanded direction. This quantity is then converted to a quaternion error. The angular rate error can be obtained from direct subtraction. The demanded torque is then expressed as

$$\tau_{\mathrm{dmd}} = -\mathbf{K}(m)\begin{bmatrix}\Delta\mathbf{q}\\ \Delta\boldsymbol{\omega}\end{bmatrix}. \tag{9}$$

The three-axes controller employed for TAM aims at tracking the attitude provided by the guidance. The inputs for this controller are: 1) the estimated attitude and angular rate, 2) the reference attitude or attitude profile. When an attitude profile is defined, the controller also accepts a reference angular rate and a reference angular acceleration ($\alpha$), which is used as part of a feedforward action. The control torque can then be expressed as

$$\tau_{\mathrm{dmd}} = -\mathbf{K}(m)\begin{bmatrix}\Delta\theta\\ \Delta\boldsymbol{\omega}\end{bmatrix} + \mathbf{I}(m)\,\alpha. \tag{10}$$

The objective of the delta-v controller is to ensure that the desired velocity vector change is achieved. It combines the single-axis controller previously presented and a thrust-controller. The inputs to the controller contain: 1) the reference delta-v vector ($\Delta v_{\mathrm{ref}}$), 2) the estimated delta-v generated since the maneuver started ($\Delta v_{\mathrm{est}}$), and 3) the attitude, angular rate vector and mass. First, the remaining delta-v vector ($\Delta v_{\mathrm{rem}}$) is calculated. The single-axis controller is then used to align the thrust vector with the direction of the remaining delta-v. When the quaternion error

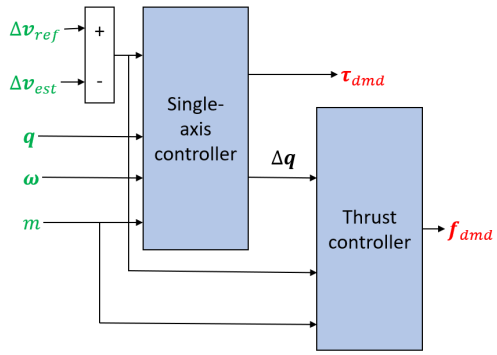


Fig. 9: Schematic view of the delta-v controller

is below a certain margin, the thrusters are activated. A fail-safe mechanism is implemented in order to stop the burn in case the attitude error with respect to the delta-v error vector exceeds a certain threshold, as it is common that during the maneuver the pointing error increases because – in the current baseline – only the attitude thrusters are used for attitude control during the orbital phase. Particularly with respect to the lunar capture maneuver, this strategy might be re-evaluated to include pulsing of the main engines as well, as is done during the powered descent. The burn is continued as soon as the pointing is aligned again.

$$\tau_{\mathrm{dmd}} = -\mathbf{K}(m)\begin{bmatrix}\Delta\mathbf{q}\\ \Delta\boldsymbol{\omega}\end{bmatrix} \tag{11}$$

$$\mathbf{f}_{\mathrm{dmd}} = \begin{cases}\mathbf{K}(m)\|\Delta\mathbf{v}\|, & \Delta\mathbf{q} \le \Delta\mathbf{q}_{\max}\\ 0, & \Delta\mathbf{q} > \Delta\mathbf{q}_{\max}\end{cases} \tag{12}$$

The delta-v controller scheme is shown in Figure 9.

### *6.2 Descent and Landing Phase*

During the Descent and Landing Phase, a controller for a 6-DoF (three translational, three rotational) vehicle model is designed. This controller aims at tracking the nominal descent trajectory from Powered Descent Initiation (PDI) to an altitude of around 300 meters over the surface of the Moon, from where an hazard avoidance maneuver (HDA) is commanded. The nominal trajectory is generated offline on ground, whereas and the hazard avoidance trajectory is computed onboard. The nominal trajectory brings the vehicle to a low vertical speed; after this is achieved, HDA mode triggered. It is meant to horizontally shift the vehicle and then land within a specific maximum horizontal radius from its actual position, avoiding specific hazards known from a pre-loaded map. The

control structure employed for HDA mode does not differ from the nominal descent controller, thus is not specifically addressed hereafter.

The designed controller operates using a cascade control approach in which the outer-loop tracks the translational reference states and the inner-loop tracks the rotational ones. When synthesizing the controllers for each loop, special care was taken to ensure a good enough frequency separation between them, in order to avoid cross-couplings between them, thus simplifying the synthesis. As the position control of the spacecraft relies on a fast attitude tracking to achieve good performance, the inner-loop cut-off frequency has to be higher than the one of the outer-loop. As the thrust vector direction in the body reference frame is fixed, the spacecraft needs to be re-oriented to be able to track the prescribed trajectory.

The inner-loop uses the same three-axes controller structure employed for TAM (see 6.1). The only difference is that an integral action is introduced to account for systematic disturbances like thruster misalignments. Furthermore, considering the specific thrusters configuration, it is worth noticing that the main thrusters have no influence on roll dynamics along the vehicle longitudinal axis. Given that the achievable roll torque from the attitude thrusters is lower, it shows convenient to tune the roll channel slightly less aggressively.

The controller for the outer-loop is designed using the following dynamics model:

$$\begin{aligned} {}^{\mathrm{MCMF}}_{\mathrm{B,MCMF}}\dot{\mathbf{r}} &= {}^{\mathrm{MCMF}}_{\mathrm{B,MCMF}}\mathbf{v} \\ {}^{\mathrm{MCMF}}_{\mathrm{B,MCMF}}\dot{\mathbf{v}} &= {}^{\mathrm{MCMF}}\mathbf{g} + \frac{{}^{\mathrm{MCMF}}\mathbf{f}}{m} - 2\,\boldsymbol{\omega}_M \times {}^{\mathrm{MCMF}}_{\mathrm{B,MCMF}}\mathbf{v} \\ &\quad - \boldsymbol{\omega}_M \times \boldsymbol{\omega}_M \times {}^{\mathrm{MCMF}}_{\mathrm{B,MCMF}}\mathbf{r} \\ \dot{m} &= -\frac{\left\| {}^{\mathrm{MCMF}}\mathbf{f} \right\|}{I_{\mathrm{sp}}\; g_0}, \end{aligned} \tag{13}$$

where MCMF refers to the Moon Centered Moon Fixed reference frame, $\mathbf{g}$ to the Moon gravitational acceleration, $\boldsymbol{\omega}_M$ to the angular rate of the MCMF frame with respect to the MCI frame, $I_{sp}$ to the specific impulse of the main engines and $g_0$ to the Earth gravity at sea level. The gravitational field model includes spherical harmonics with degree and order equal to five. This dynamics model is linearized numerically at multiple points of the nominal trajectory. The outer-loop consists of a feedback loop with a feedforward action, that tracks velocity and position of the nominal trajectory.An integral action is added

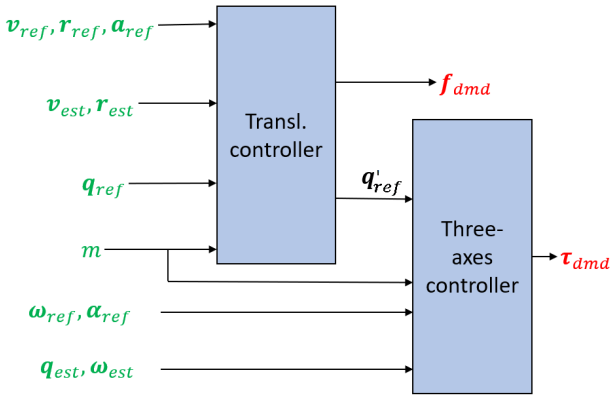


Fig. 10: Schematic view of the 6-DoF controller

here too, similarly to the inner loop, to minimize the the steady-state position error.

The equations of the outer- and inner-loop controllers are then

$$\mathbf{f}_{\mathrm{dmd}} = -\,\mathbf{K}(m) \begin{bmatrix} \int \Delta\mathbf{r} \\ \Delta\mathbf{r} \\ \Delta\mathbf{v} \end{bmatrix} + m\,\mathbf{a} \tag{14}$$

$$\tau_{\mathrm{dmd}} = -\,\mathbf{K}(m) \begin{bmatrix} \int \Delta\theta \\ \Delta\theta \\ \Delta\omega \end{bmatrix} + \mathbf{I}(m)\,\alpha. \tag{15}$$

The structure of the controller is shown in Figure 10; the reference $\mathbf{q}'_{\mathrm{ref}}$ is computed as

$$\mathbf{q}'_{\mathrm{ref}} = \mathbf{q}_{\mathrm{ref}} \odot \mathbf{q}_{\mathrm{corr}}, \tag{16}$$

where $\mathbf{q}_{\mathrm{corr}}$ is an attitude correction needed to track the trajectory position, and $\odot$ is the quaternion multiplication as defined in Equation D-8 of [12]. The term $\mathbf{q}_{\mathrm{corr}}$ is the quaternion obtained from the rotation vector [11] that transforms the vehicle longitudinal axis into $\mathbf{f}_{\mathrm{dmd}}$ vector direction.

The frequency separation between inner- and outer-loop was analyzed by studying the closed-loop behavior of the linearized systems in the frequency domain. The cutoff frequency of the inner-loop varies (due to mass changes) between 0.2 and 0.3 Hz (only pitch/yaw channels), between 0.08 and 0.17 Hz for the roll channel, while that of the outer-loop varies between 0.03 and 0.06 Hz. Simulations shown in Section 9 evidence that this separation provide good landing performance. In addition, the bandwidth of the controller was compared with the bandwidth of the sloshing effect, shown in Figure 11, with the objective of

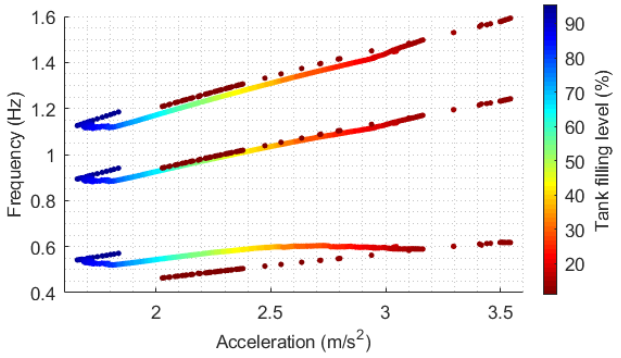


Fig. 11: Sloshing frequencies as function of the vehicle's acceleration and the tank filling level

ensuring that the control system is slower than the first sloshing mode. This choice is to avoid that the control encourages slosh dynamics along the powered descent and landing. In terms of performance, LQR synthesis guarantees a phase margin for both loops of at least 55° (assuming control channels are analyzed independently). Considering the whole MIMO system, the maximum tolerable input-multiplicative perturbation threshold for both loops (as defined in [13]) is about 0.8.

## 7. Actuator Management

The thrust and torques for attitude, position and delta-v control need to be delivered to the spacecraft by the main engines and attitude control thrusters. All thrusters contribute to both the generation of forces and the generation of torques. The allocation of demanded forces and torques is achieved by solving an optimization problem.

### *7.1 Control allocation*

The non-pulsable (NP) main engines are switched on in MEM and PDM only; they can be deactivated for thrust ramp-down shortly before touchdown (in PDM) and during spacecraft re-pointing (in MEM). For this reason, the control allocation only utilizes the pulsable engines and attitude control thrusters, while still accounting for any NP engine contribution.

The spacecraft has a set of $n = 16$ considered thrusters (eight pulsable main engines and eight attitude control thrusters), which can mathematically be described as a set of $n$ force vectors applied in $n$ geometric locations with respect to the center of mass of the spacecraft. This defines $n$ pairs

$$\mathscr{T}_i \triangleq \left(\mathbf{r}_i, \mathbf{f}_{\mathrm{thr}_i}\right),\ i = 1,\ldots,n \tag{17}$$

where $\mathbf{r}_i$ is the position of the $i$-th thruster and $\mathbf{f}_{\mathrm{thr}_i}$ the force produced by the $i$-th thruster on the vehicle. Note that each of the thrusters has a lever arm with respect to the center of mass, therefore it generates a torque around the center of mass expressed as:

$$\tau_{\mathrm{thr}_i} = \mathbf{r}_i \times \mathbf{f}_{\mathrm{thr}_i},\ i = 1,\ldots,n. \tag{18}$$

The control allocation has to define, in a continuous domain, the amount of thrust $\mathbf{f}_{\mathrm{thr}_i}$ that each single thruster needs to generate to meet the control force and torque demands. The problem can be understood as the minimization of the addition of three cost terms:

$$J_1 = \left\| \sum_{i=1}^{n} \mathbf{f}_{\mathrm{thr}_i} - \mathbf{f}_{\mathrm{dmd}} \right\|, \tag{19}$$

$$J_2 = \left\| \sum_{i=1}^{n} \tau_{\mathrm{thr}_i} - \tau_{\mathrm{dmd}} \right\|, \tag{20}$$

$$J_3 = \left\| \sum_{i=1}^{n} \mathbf{f}_{\mathrm{thr}_i} \right\|, \tag{21}$$

where $\mathbf{f}_{\mathrm{dmd}}$ is the demanded control force and $\tau_{\mathrm{dmd}}$ the demanded control torque. Note that $J_3$ expresses the need of selecting the solution among the possible ones that minimizes fuel consumption.

The solution of the problem has been approached using a Linear Programming formulation. The joined cost functions can be expressed as

$$J = \sum_{i=1}^{n} \mathbf{q}_i + \lambda_F s_F + \lambda_T s_T, \tag{22}$$

where $\mathbf{q}_i$ represents the normalized thruster-specific thrust solution and $s_f$ and $s_t$ are slack variables. The constants $\lambda_F$ and $\lambda_T$ are penalty weights. The optimization vector is defined as $\mathbf{x} = [\mathbf{q}_1, ..., \mathbf{q}_n, s_F, s_T]$.

The optimization has to respect some constraints: Firstly,

$$\mathbf{A}_{\mathrm{eq}}\,\mathbf{x} = \mathbf{b}_{\mathrm{eq}}, \tag{23}$$

$$\mathbf{A}_{\mathrm{eq}} = \begin{bmatrix} \bar{\mathbf{f}}_{\mathrm{thr}_1} & \cdots & \bar{\mathbf{f}}_{\mathrm{thr}_n} & \mathbf{f}_{\mathrm{dmd}} & 0 \\ \mathbf{r}_{\mathrm{thr}_1} & \cdots & \mathbf{r}_{\mathrm{thr}_n} & 0 & \tau_{\mathrm{dmd}} \end{bmatrix}, \tag{24}$$

$$\mathbf{b}_{\mathrm{eq}} = \begin{bmatrix} \mathbf{f}_{\mathrm{dmd}} \\ \tau_{\mathrm{dmd}} \end{bmatrix}. \tag{25}$$

Here, $\bar{\mathbf{f}}_{\mathrm{thr}_i}$ is the $i$-th thruster maximum thrust and $\mathbf{f}_{\mathrm{dmd}}$ the demanded control force. This is equivalent to imposing:

$$\begin{array}{rcl} \sum_{i=1}^{n} \mathbf{f}_{\mathrm{thr}_i} & = & (1-s_F)\,\mathbf{f}_{\mathrm{dmd}} \\ \sum_{i=1}^{n} \mathbf{t}_{\mathrm{thr}_i} & = & (1-s_T)\,\tau_{\mathrm{dmd}}. \end{array} \tag{26}$$

The slack variables act as leakage terms in case the constraints cannot be satisfied, which is never the case for well posed force-torque demands.

In addition, $\mathbf{q}_i$ must be less than or equal to one, such that the force produced by each thruster does not exceed its capability. This translates into the following constraint:

$$\mathbf{A}_{\mathrm{le}}\,\mathbf{x} \leq \mathbf{b}_{\mathrm{le}}, \tag{27}$$

where

$$\begin{array}{l} \mathbf{A}_{\mathrm{le}} = \mathbf{I}_{\mathrm{n+2}} \\ \mathbf{b}_{\mathrm{le}} = \mathbf{1}_{\mathrm{n+2}}. \end{array} \tag{28}$$

and $\mathbf{I_{n+2}}$ is the identity matrix having dimensions $[(n+2)\times(n+2)]$, and $\mathbf{1}^{n+2}$ is a $[(n+2)\times 1]$ column vector having all the entries equal to 1. This ensures that

$$\left\{ \begin{array}{rcccl} 0 & \leq & \bar{\mathbf{f}}_{\mathrm{thr}_i}\,\mathbf{q}_i & \leq & \bar{\mathbf{f}}_{\mathrm{thr}_i} \\ 0 & \leq & (\mathbf{r}_i \times \bar{\mathbf{f}}_{\mathrm{thr}_i})\,\mathbf{q}_i & \leq & \bar{\tau}_{\mathrm{thr}_i}. \end{array} \right. \tag{29}$$

The problem is then solved using the *Two-Phases SIMPLEX algorithm* [14, 15]. The positiveness of the solution does not have to be explicitly accounted for as a constraint, because the chosen method automatically guarantees this by construction. The resulting $\mathbf{q}_i$ are then realized by the thruster management.

### *7.2 Thruster management*

The thruster management contains a Pulse Width Modulation (PWM) algorithm and a scheduling algorithm. It considers the minimum allowed on/off times of the thrusters and limitations on how many engines can be switched from off to on or vice-versa $n_{\mathrm{thr,interval}}$ inside a specific time interval $dt_{\mathrm{interval}}$ to avoid causing spikes in the propellant pressurization system. It is running with the actuator command frequency $dt_{\mathrm{cmd}}$ and outputs the commanded switch-on time vector $\mathbf{t}_{\mathrm{on,cmd}}$ (relative to the beginning of each actuator command window) and the on-time duration vector $\Delta t_{\mathrm{cmd}}$.

First, the demanded force of each thruster is convert into the corresponding demanded on-time $\Delta t_{\mathrm{dmd}}$:

$$\Delta t_{\mathrm{dmd}} = \frac{\mathbf{f}_{\mathrm{dmd}}}{\mathbf{f}_{\mathrm{thr}}} \cdot dt_{\mathrm{cmd}} \tag{30}$$

Next, the commanded switch-on times $\mathbf{t}_{\mathrm{on,cmd}}$ and the commanded on-time durations $\Delta t_{\mathrm{cmd}}$ are scheduled by chronologically looking through the available scheduling slots inside the current command window and evaluating which thrusters have to be switched. This evaluation is done in two steps: First, each thruster's current on/off state $\mathbf{x}_{\mathrm{curr}}$ and demanded on/off state $\mathbf{x}_{\mathrm{dmd}}$ for the currently evaluated scheduling slot are compared:

$$\mathbf{b}_{\mathrm{switch}} = \mathbf{x}_{\mathrm{dmd}} \oplus \mathbf{x}_{\mathrm{curr}} \tag{31}$$

Then several conditions are checked, of which all have to be fulfilled for the switch to be considered. If a thruster needs to be switched on, the switch is only considered if the demanded on-time is more than half the minimum on-time. If a thruster needs to be switched off, the switch is only considered if the minimum on-time is respected and the switch-off occurs more than half the minimum off-time before the end of the current command cycle. This way, the algorithm avoids switching off thrusters very shortly before the end of a command cycle and thereby reducing their availability in the next cycle.

Each switching slot can only contain one thruster switch but several slots can be assigned to the same time. The current slot is assigned to the thruster with the largest on-time error $\Delta t_{\mathrm{err}}$. For thrusters which need to be switched on, the error is defined as

$$\Delta t_{\mathrm{err}} = \Delta t_{\mathrm{dmd}} - (dt_{\mathrm{cmd}} - t_{\mathrm{slot}_i}) \tag{32}$$

with $t_{\mathrm{slot}_i}$ being the time of the currently considered switching slot (relative to the beginning of the current actuator command window) and $i$ being the index of the current slot. Note that in this case, the error is commonly negative, which means that a perfect realization of the demanded on-time is still possible.

For thrusters which need to be switched off, the error is defined as

$$\Delta t_{\mathrm{err}} = \Delta t_{\mathrm{curr}} - \Delta t_{\mathrm{dmd}} \tag{33}$$

with $\Delta t_{\mathrm{curr}}$ being the on-time durations achieved at the currently considered switching slot. In this case, the error is always larger or equal to zero, as only thrusters which have reached their demanded on-time are considered.

It is worth noting that the switching slots are not equally spaced but that their times are instead defined by the times previous thruster switches have occurred,

such that the current available slot time becomes:

$$t_{\text{slot}_i} = t_{\text{slot}_{i-n_{\text{thr,interval}}}} + dt_{\text{interval}} \tag{34}$$

If no thruster switches are required at this time, the slot time will be set to the next time a thruster switch is required.

## 8. Simulation environment

In this section, an overview of the simulation environment developed in Simulink (Figure 12) and used to analyze the performance of the control system is provided. The topics covered are: 1) characteristics of the vehicle, 2) modeling of external disturbances, 3) uncertainties in the model and 4) additional on-board software.

The propulsion system was modeled as presented in section 5.1. The navigation system contains the following set of sensors: 1) one three axes Inertial Measurement Unit (IMU), 2) ten sun sensors, 3) two star trackers, 4) two altimeters, 5) one radar velocity meter with three beams and 6) the Crater Navigation system (CNav). CNav provides an estimate of the absolute position and attitude, using an algorithm to detect and match craters on images from an on-board camera with a crater catalog [16, 17].

The external forces and torques considered are those originating from: 1) Earth's gravity, 2) Moon's gravity, 3) Earth's atmosphere and 4) solar radiation pressure. The model used for Earth's gravity is the Earth Gravity Model EGM2008 [18] of sixth degree and sixth order, modeling also the gravity gradient. For the gravity of the Moon the GRGM660PRIM model [19] of fifth degree and fifth order is used. The Harris-Priester model [20] is used to obtain the atmospheric density (only considered for Low Earth Orbit (LEO)). The spacecraft is modeled as an octahedron prism and the distributed force over each surface in contact with the atmosphere integrated to obtain the total force and torque. In order to obtain the solar radiation disturbances, first it is checked if the spacecraft is in eclipse (due to Moon or Earth). The solar radiation pressure is then computed and the force and torque integrated in the same way as for the atmospheric disturbance.

The control system needs to be robust against a defined level of uncertainty, understanding uncertainty as the difference between the nominal models used for GNC function development and tuning, and reality. This uncertainty can be divided in the following groups: 1) mass uncertainties, 2) propulsion system uncertainties and 3) sensor uncertainties. The mass uncertainty refers not only to uncertainty in the mass but also in the moment of inertia and the center of mass. The uncertainty in the propulsion system is related to the dynamics of each thruster (e.g. maximum thrust, time to 90 % thrust and noise) and to its position and orientation. The uncertainty related to the sensors is related to their position and orientation as well as their measurement noise. The simulation environment allows to run Monte-Carlo campaigns, varying all these uncertainties.

The guidance and navigation systems are incorporated in the simulation. The guidance system generates a signal to be tracked by the control system. It contains several guidance modes for the different AOCS modes. The navigation system contains estimations of several variables, including 1) the mass properties, estimated using propellant consumption and relation between thrust and acceleration, 2) attitude and angular rate, 3) position, velocity and acceleration (only for the powered descent), 4) delta-v (only for the delta-v maneuvers) and 5) altitude (only for the powered descent). The Mission Vehicle Management (MVM) uses the navigation estimates and telemetry commands to activate/deactivate AOCS modes.

## 9. Test Results

This section presents preliminary test results for each AOCS mode, with a focus on the most demanding phases of the mission: 1) delta-v maneuvers and 2) Powered Descent, Hazard Avoidance and Landing.

An example for a delta-v maneuver is shown in Figure 13. In this figure, the different phases of this maneuver are clearly visible. First, the vehicle is aligned with the desired thrust direction. Once this alignment is achieved within a certain accuracy, the thrusters are activated, generating a delta-v. During the thrusting, the alignment accuracy degrades due to the offset between center of mass and center of thrust. If this degradation goes beyond 1°, the thrusters are deactivated and the vehicle is re-aligned. This process is repeated as many times as necessary until the delta-v is achieved within a defined margin.

Figure 14 shows the delta-v achieved for twenty simulations as part of a small Monte-Carlo campaign.

During the Powered Descent maneuver, the controller aims at correcting for the initial error in position and velocity at PDI, while counteracting the

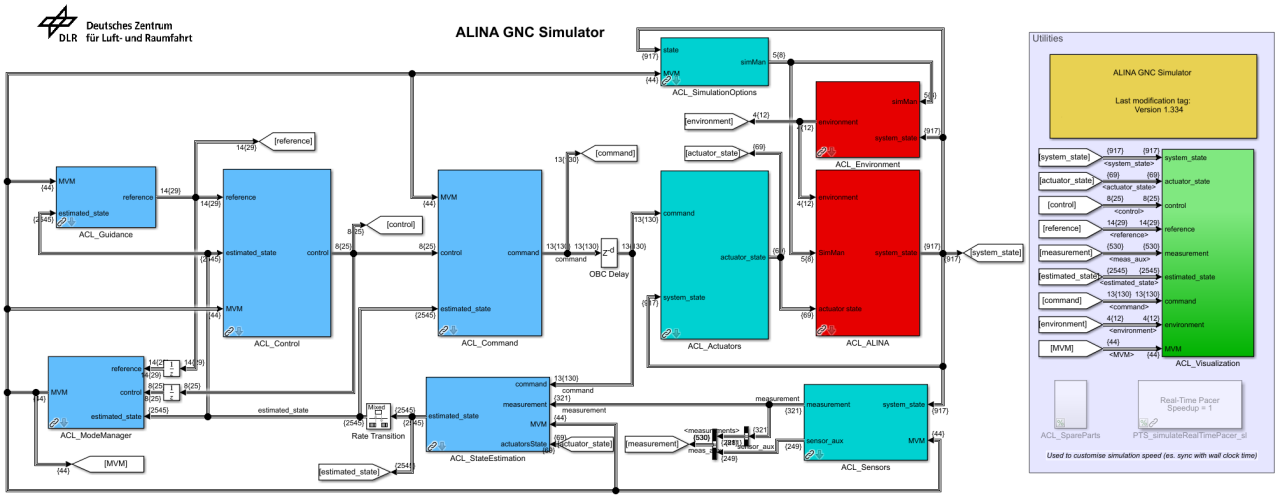


Fig. 12: View of the full Simulink GNC simulator environment

effect of disturbances. Figure 15 shows the results of a small Monte-Carlo campaign of 20 runs. It can be seen that the actual trajectory of each simulation converges to the nominal trajectory, despite the initial errors.

Figure 16 shows the control error in position and velocity for the same simulation campaign shown in Figure 15. It can be seen that the errors in position and velocity converge to small values by the middle of the descent: approx. 20 m of position error and 1 m/s in velocity error. Several sudden peaks in error can be seen, particularly in position. These peaks are caused by jumps in the navigation estimate: The navigation filter uses DLR's CNav [16] for determining the spacecraft's position relative to the lunar surface. These measurements, however, become unavailable if there are no craters in the field of view of the camera, either because of flying over mountainous areas or because of large attitude offsets to compensate large lateral position/velocity errors. In the time CNav is unavailable, the position estimate starts drifting. As soon as CNav becomes available again, the position estimate jumps, leading to a jump in the control error, as the control system was previously minimizing the error according to the drifted position estimate. For some of the simulations, CNav acquires for the first time some considerable time into the simulation. One example for this behavior is a simulation result plotted in purple (in Figure 15 and 16), which shows a large actual altitude error for a considerable amount of time and shows a strong peak in control error at 220 s. CNav does not acquire in the 30 s of simulation time before the PDHL is started. A large estimated lateral position error then leads to a large attitude movement to redirect the thrusters to correct for it. Consequently, the CNav camera loses sight of the lunar surface. In this moment, the very rough initialization value for the position estimate (based on orbit determination via ranging) is used and propagated until CNav becomes available. This will be avoided during the actual mission because the navigation filter will be started a much longer time before PDHL than in these simulations. To optimize the final landing accuracy, it is advisable to consider crater visibility for the CNav camera for the trajectory design, in particular for the last part of it (approx. 25 %). For the first ALINA mission, this was not required, as the final landing accuracy lies well inside the requirement, despite the intermittent CNav availability.

In Figure 16, it is also noticeable that the error decreases considerably during the last 20-30 seconds of the trajectory. This is the final part of the descent, during which the hazard avoidance takes place. During the hazard avoidance, a new reference trajectory, from the current estimated position and velocity to a safe landing site, is computed on-board. Figure 17 shows an example of the detumbling maneuver after separation. In this simulation, the vehicle has an initial angular rate of approximately 20 °/s. With the baselined thruster configuration, the detumbling maneuver lasts around 50 seconds.

Figure 18 shows a re-pointing maneuver, in which

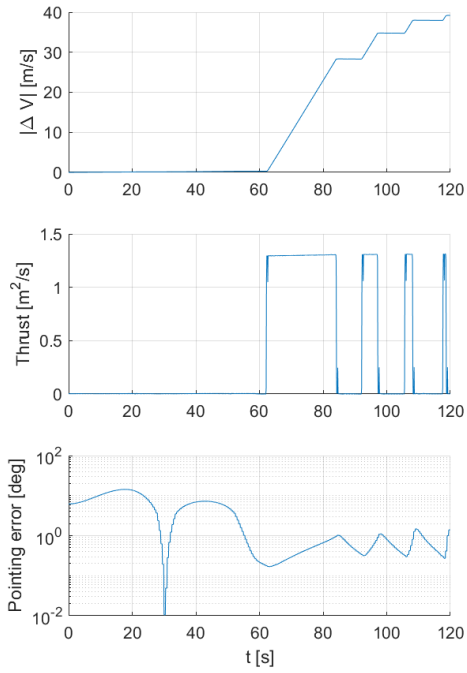


Fig. 13: Delta-v maneuver

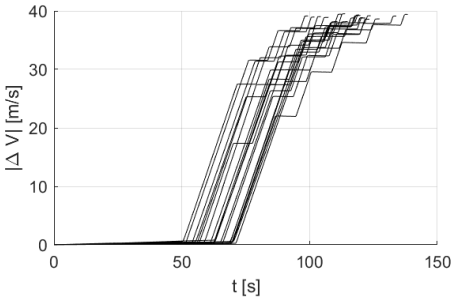


Fig. 14: Delta-v achieved over 20 runs.

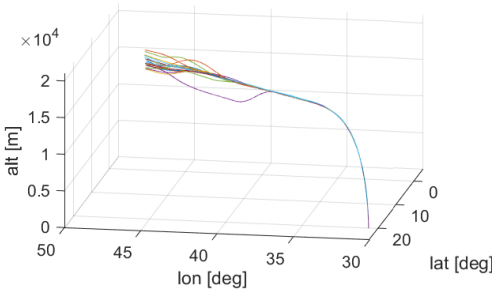


Fig. 15: Powered Descent trajectory (20 runs)

the objective is to align the vehicle with a defined axis, while slowly turning around the pointing axis. It can be seen that the first part of the maneuver (approx. 30 seconds) consists of a big change in the attitude of the vehicle, while the rest aims at maintaining the alignment.

Figure 19 shows an example of the 3-axes controller performance when a constant attitude is commanded. It can be seen that limit-cycling occurs with a frequency of approx. 0.025 Hz between the limits of the deadband. The deadband and controller gains can be tuned according to the particular requirements of the different phases of the mission.

As explained in Section 5.2, a model capable of simulating propellant sloshing dynamics has been implemented. This model is employed to simulate with enhanced accuracy the vehicle dynamics during the accelerated phases, the most important one occurring with the Powered Descent, HDA & Landing (PDHL). The model embeds three sloshing modes per tank. In this scenario, only half of the tanks are full, as a large amount of propellant is already spent during the earth orbit raising and the lunar orbit injection. The comparison between two simulations is presented here to show how the control system copes with sloshing disturbances. In the first simulation, the PDHL is simulated using nominal parameters with the sloshing dynamics model in the loop. The second simulation uses the 6-DoF rigid body model. The two resulting time series of the position error are then compared: Figure 20 shows the norm of the difference between the two. The main outcome is that the plot keeps bounded during the entire PDHL, showing that the controller can keep the effect of these disturbances moderated, and that the maximum induced error is relatively low ($\approx$ 10 meters).

## 10. Conclusion

This paper presented the control system design for the ALINA lunar lander. This system successfully completed the Preliminary Design Review for PTS's first ALINA mission. It is also used as a flexible blue print for rapid prototyping for future Moon missions, as it can be quickly adapted to different lunar mission scenarios, including different vehicles. It is divided into two main subsystems: 1) control function and 2) control allocation and actuator management. The

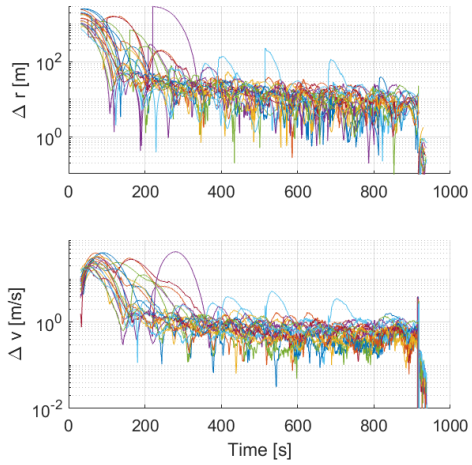


Fig. 16: Control error during PDM (20 runs)

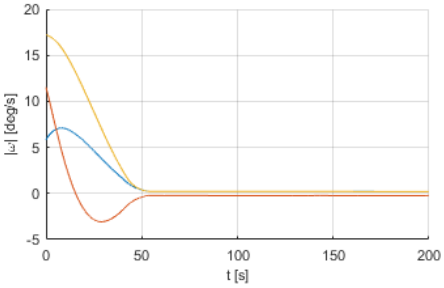


Fig. 17: Simulation result for detumbling controller

control function contains multiple controllers, which comply with all the applicable requirements of the different mission phases. All of these controllers are developed by linearizing the dynamics of the vehicle at several points of the trajectory. The linearized dynamics are then used to compute an optimal control gain using a linear-quadratic regulator. The resulting gains are scheduled based on the estimated mass. The actuator management is addressed as a Linear Programming problem, which is solved using a SIMPLEX algorithm. The implementation of this algorithm also complies with all applicable nominal requirements.

### *10.1 Next steps and improvements*

Several improvements to the proposed design are envisioned:

- analyze performance improvements when using alternative control theories, particularly robust control;
- perform a more extended Monte-Carlo campaign using the augmented model with sloshing dynamics to better asses control system performance in presence of both uncertainties and sloshing disturbances;
- extend the control allocation strategy to support Failure Detection, Isolation, and Recovery (FDIR) scenarios to maintain control of the vehicle when a single or multiple thrusters are not operational.

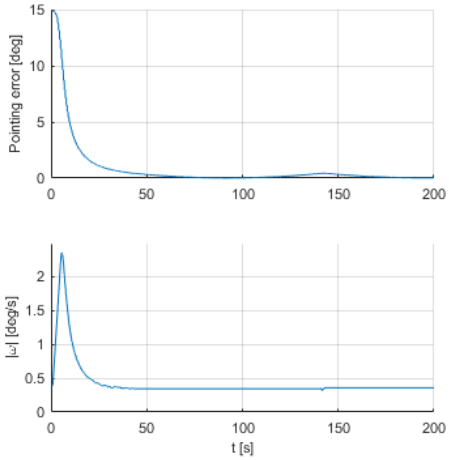


Fig. 18: Simulation result for the single-axis controller

## References

[1] K. Becker and K. A. Gray, "Back to Apollo 17 with PTScientists' Mission-1," in *Proceedings of Global Space Exploration Conference (GLEX), Beijing*, 2017.

[2] J. Eyer, C. Hervieu, M. Wagener, V. Still, E. Hill, D. Bryson, R. Court, C. Gopal, T. Flecht, M. Scherrmann, L. Steindorf, H. Krüger, and M. Winter, "ALINA-2: Innovations on Planetary Transportation Systems GmbH's Commercial Lunar Lander," *New Space*, vol. 9, 2021. [Online]. Available: https://doi.org/10.1089/space.2020.0005

[3] M. Winter, H. Krüger, S. Farì, J. L. Redondo, B. Razgus, S. Woicke, D. Seelbinder, A. Wenzel, S. Theil, B. Maass, M. Sagliano, G. F.

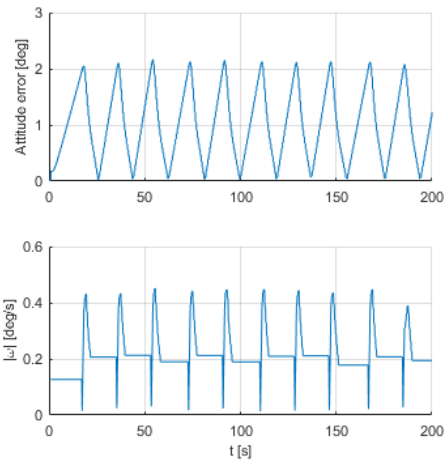


Fig. 19: Simulation result for the 3-axes controller

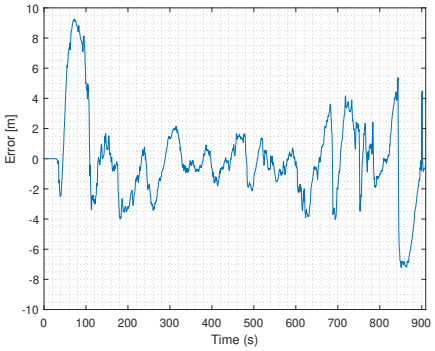


Fig. 20: Effect of sloshing, in a nominal simulation setup. Here, the position errors resulting from two different simulations (one with and one without sloshing model) are compared and their difference is shown in terms of 2-norm

Trigo, A. Heidecker, R. Schwarz, and S. Bremer, "ALINA Moon Lander GNC – Architecture, Design and Test Results," in *11th International ESA Conference on Guidance, Navigation & Control Systems*, 2021, p. 18.

[4] N. M. Dick, "Development and Verification of a Continuous Estimation of Fuel Reserves and Dynamic Mass Properties of a Space Vehicle," Master's thesis, University of Bremen, 2020.

[5] J. A. Frosch and D. P. Vallely, "Saturn AS-501/S-IC flight control system design." *Journal of Spacecraft and Rockets*, vol. 4, no. 8, pp. 1003–1009, 1967.

[6] H. N. Abramson, "Dynamic behavior of liquids in moving containers with applications to space vehicle technology," NASA, Washington DC, Special Publication (SP) 19670006555, 1966.

[7] T. A. Lance, "Analysis of Propellant Slosh Dynamics and Generation of an Equivalent Mechanical Model for Use in Preliminary Voyager Autopilot Design Studies," NASA, Technical Memorandum 19680017770, 1966.

[8] O. Bayle, V. L'Hullier, M. Ganet, P. Delpy, J.-L. Francart, and D. Paris, "Influence of the ATV Propellant Sloshing on the GNC Performance," in *AIAA Guidance, Navigation, and Control Conference and Exhibit*. Monterey, California: American Institute of Aeronautics and Astronautics, Aug. 2002.

[9] S. Farì, D. Seelbinder, and S. Theil, "Advancing Modeling and Simulation of Vertical Landing Vehicles with Fuel Slosh Dynamics," *Paper submitted for publication*, 2021.

[10] F. T. Dodge *et al.*, *The new "Dynamic behavior of liquids in moving containers"*. Southwest Research Inst. San Antonio, TX, 2000.

[11] F. L. Markley and J. L. Crassidis, *Fundamentals of spacecraft attitude determination and control*. Springer, 2014.

[12] J. R. Wertz and C. S. Corporation, Eds., *Spacecraft Attitude Determination and Control*, 1st ed., ser. Astrophysics and Space Science Library. Dordrecht: Kluver Acad. Publ, 2002, no. 73.

[13] J. B. Burl, *Linear Optimal Control: $H_2$ and $H_\infty$ methods*. Addison-Wesley Longman Publishing Co., Inc., 1998.

[14] F. Hillier and G. J. Lieberman, *Introduction To Operations Research*, 10th ed. McGraw-Hill Education, 2015.

[15] J. Nocedal and S. J. Wright, *Numerical Optimization*, ser. Springer Series in Operations Research. New York: Springer, 1999.

[16] B. Maass, S. Woicke, W. M. Oliveira, B. Razgus, and H. Krüger, "Crater navigation system for autonomous precision landing on the moon," *Jour-*

*nal of Guidance, Control, and Dynamics*, pp. 1–18, 2020.

[17] G. F. Trigo, B. Maass, H. Krüger, and S. Theil, "Hybrid optical navigation by crater detection for lunar pin-point landing: trajectories from helicopter flight tests," *CEAS Space Journal*, vol. 10, no. 4, pp. 567–581, 2018.

[18] N. K. Pavlis, S. A. Holmes, S. C. Kenyon, and J. K. Factor, "The development and evaluation of the earth gravitational model 2008 (egm2008)," *Journal of geophysical research: solid earth*, vol. 117, no. B4, 2012.

[19] F. G. Lemoine, S. Goossens, T. J. Sabaka, J. B. Nicholas, E. Mazarico, D. D. Rowlands, B. D. Loomis, D. S. Chinn, G. A. Neumann, D. E. Smith *et al.*, "Grgm900c: A degree 900 lunar gravity model from grail primary and extended mission data," *Geophysical research letters*, vol. 41, no. 10, pp. 3382–3389, 2014.

[20] D. L. Dowd and B. Tapley, "Density models for the upper atmosphere," *Celestial mechanics*, vol. 20, no. 3, pp. 271–295, 1979.